# Analysis and Optimization of Variable-Frequency Soft-Switching Peak Current Mode Control Techniques for Microinverters

S. Milad Tayebi, *Student Member, IEEE*, and Issa Batarseh, *Fellow, IEEE*

***Abstract*—This paper presents a detailed power loss model for a microinverter with three different zero voltage switching boundary conduction mode (BCM) current modulation methods. The model is used to calculate the optimum peak current boundaries for each modulation method. Based on the power loss model, a dual-zone modulation method is proposed to further improve the microinverter efficiency. The proposed modulation method provides two main benefits: the addition of one more soft switching transition and low inductor peak current. The additional soft switching transition reduces switching losses by means of zero current switching. The lower peak current boundary reduces inductor rms current and conduction losses as well as allowing the output filter inductor to be smaller and more efficient. An improved BCM peak current control method was proposed and implemented on a microinverter prototype. The control circuit provides a highly accurate representation of the filter inductor current waveform and also provides galvanic isolation that simplifies control circuit design. The experimental results on a 400-W three-phase half-bridge microinverter validate the theoretical analysis of the power loss distribution and demonstrate that further improvement in efficiency can be achieved by using the proposed dual-zone modulation method.**

***Index Terms*—Boundary conduction mode (BCM), microinverters, power loss analysis, soft switching, three-phase inverters, zero voltage switching (ZVS), zero current switching (ZCS).**

## I. Introduction

INVERTERS are widely used in photovoltaic (PV) based power generation systems. Most of these systems have been based on medium to high power string inverters [1], [2]. Microinverters have been shown to have advantages over their string inverter counterparts in both grid-tied PV energy harvesting and standalone microgrid systems with energy storage [3]–[6]. Some of these advantages are simplified installation, elimination of high-voltage dc wiring, higher system reliability, and improved energy harvesting.

In low-power applications such as solar microinverters, increasing the switching frequency can reduce the size of passive components resulting in higher power density [7]. However, switching losses and electromagnetic interference may increase as a consequence of higher switching frequency. Soft switching techniques have been proposed to overcome these issues [8], [9].

Zero voltage switching (ZVS) boundary conduction mode (BCM) peak current control is a promising soft switching candidate for low power applications where the switching losses are usually dominant [10]–[12]. For this purpose, three different peak current mode control methods have been introduced in [13]: BCM with fixed reverse current, BCM with variable reverse current, and BCM with fixed bandwidth. In these modulation methods, the inductor current is bidirectional during switching cycle to achieve turn-on ZVS. Although BCM control results in increased rms current, conduction losses and core losses when compared with continuous-conduction mode, switching losses are greatly reduced.

In this paper, a detailed power loss analysis has been conducted for each of the three above-mentioned modulation techniques. The optimum tradeoff between switching frequency and inductor rms current value is determined using the power loss model in order to maximize efficiency. In an effort to further improve efficiency, a dual-zone modulation method along with an improved control method are proposed and implemented. The primary benefits of the proposed control technique are an additional soft switching transition and low inductor peak current.

This paper first introduces three different BCM peak current mode control methods. A detailed power loss model is presented in Section III in order to calculate the optimum peak current boundaries for each modulation method. Based on the power loss model, the proposed dual-zone modulation method is presented in Section IV. Section V introduces the improved BCM peak current control. The experimental results in Section VI verify the accuracy of the loss model and demonstrate that further improvement in efficiency can be achieved by using the proposed dual-zone modulation method. The conclusion is in the last section.

## II. Variable-Frequency Peak Current Mode Control Techniques

Three ZVS BCM peak current mode control methods are described and compared in this section. Fig. 1 depicts a standard power circuit of a three-phase half-bridge inverter. The body

Manuscript received August 3, 2016; revised November 9, 2016; accepted February 18, 2017. Date of publication March 1, 2017; date of current version November 2, 2017. This work was supported in part by the U.S. Department of Energy under Grant DE-EE0003176 and in part by the National Science Foundation under Grant ECCS-1156633. Recommended for publication by Associate Editor Y. Shimizu.

The authors are with the Department of Electrical Engineering and Computer Science, University of Central Florida, Orlando, FL 32826 USA (e-mail: tayebi@knights.ucf.edu; batarseh@ucf.edu).

Color versions of one or more of the figures in this paper are available online at http://ieeexplore.ieee.org.

Digital Object Identifier 10.1109/TPEL.2017.2676097

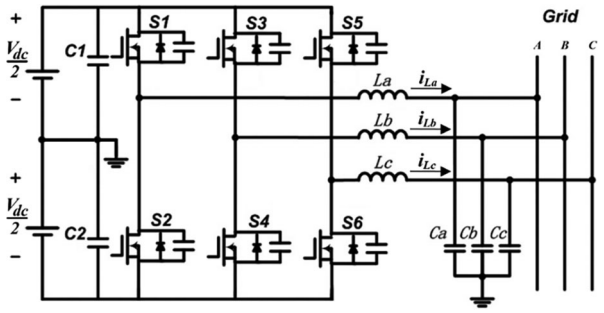


Fig. 1. Three-phase half-bridge inverter.

diode and the parasitic capacitance of the MOSFETs help to achieve ZVS in an inverter output stage. In order to implement turn-on ZVS, the bidirectional inductor current discharges the MOSFET parasitic capacitance until its body diode conducts prior to each switching transition.

In order to inject ac current into the grid, the average inductor current must be equal to the reference current during each switching cycle. Therefore, the inductor current has to be between two predetermined boundaries. Three current modulation methods with different boundary shapes have been introduced in [13], which satisfy this requirement: BCM with fixed reverse current, BCM with variable reverse current, and BCM with fixed bandwidth.

As shown in Fig. 2, the inductor current has to be between the upper and lower limits for all the three modulation techniques in order to generate an average current equal to the reference current. Since the inverter power loss is to be analyzed in this paper, the inductor current and switching frequency are calculated for each of the three modulation techniques.

The upper and lower boundaries and switching frequency for BCM with fixed reverse current modulation can be calculated as follows:

$$\begin{cases} I_{\text{upper}} = 2I_{\text{REF}} \sin(\omega t) + I_o \\ I_{\text{lower}} = -I_o \end{cases}, \text{ if } \sin(\omega t) \geq 0$$

$$\begin{cases} I_{\text{upper}} = I_o \\ I_{\text{lower}} = 2I_{\text{REF}} \sin(\omega t) - I_o \end{cases}, \text{ if } \sin(\omega t) < 0 \quad (1)$$

$$f_{\text{sw}}(t) = \frac{\left(V_{\text{dc}}/2\right)^2 - (V_m \sin(\omega t))^2}{LV_{\text{dc}}\left(2I_{\text{REF}} \sin(\omega t) + 2I_o\right)} \quad (2)$$

where, $I_{\text{REF}}$ is the output peak current reference, $I_o$ is the reverse current for achieving ZVS, $V_{\text{dc}}$ is the input voltage for the half-bridge inverter, $V_m$ is the grid or output peak voltage, and $L$ is the output filter inductor.

The boundaries and switching frequency for BCM with variable reverse current modulation can be found as

$$\begin{cases} I_{\text{upper}} = \frac{3}{2} I_{\text{REF}} \sin(\omega t) + I_o \\ I_{\text{lower}} = \frac{1}{2} I_{\text{REF}} \sin(\omega t) - I_o \end{cases}, \text{ if } \sin(\omega t) \geq 0$$

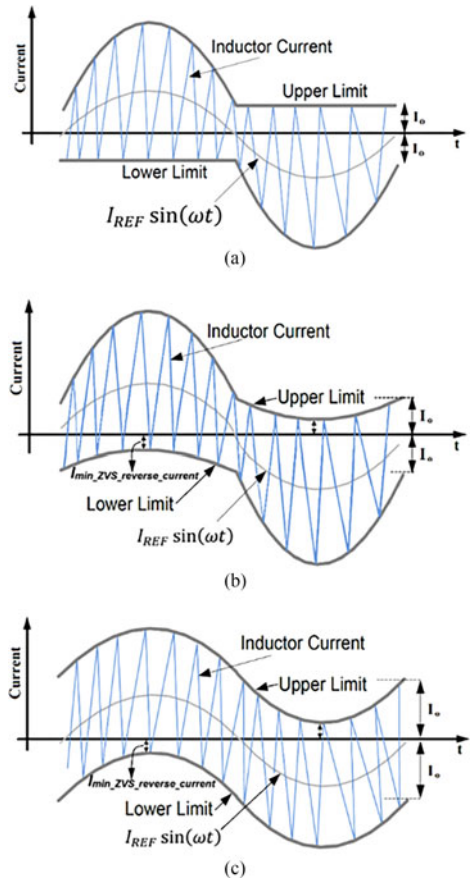


Fig. 2. Three different ZVS BCM modulation methods: (a) fixed reverse current, (b) variable reverse current, (c) fixed band width.

$$\begin{cases} I_{\text{upper}} = \frac{1}{2} I_{\text{REF}} \sin(\omega t) + I_o \\ I_{\text{lower}} = \frac{3}{2} I_{\text{REF}} \sin(\omega t) - I_o \end{cases}, \text{ if } \sin(\omega t) < 0 \quad (3)$$

$$f_{\text{sw}}(t) = \frac{\left(V_{\text{dc}}/2\right)^2 - (V_m \sin(\omega t))^2}{LV_{\text{dc}}\left(I_{\text{REF}} \sin(\omega t) + 2I_o\right)}. \quad (4)$$

The upper and lower limits and switching frequency for BCM with fixed bandwidth modulation can be expressed as follows:

$$\begin{cases} I_{\text{upper}} = I_{\text{REF}} \sin(\omega t) + I_o \\ I_{\text{lower}} = I_{\text{REF}} \sin(\omega t) - I_o \end{cases}, \text{ if } \sin(\omega t) \geq 0$$

$$\begin{cases} I_{\text{upper}} = I_{\text{REF}} \sin(\omega t) + I_o \\ I_{\text{lower}} = I_{\text{REF}} \sin(\omega t) - I_o \end{cases}, \text{ if } \sin(\omega t) < 0 \quad (5)$$

$$f_{\text{sw}}(t) = \frac{\left(V_{dc}/2\right)^2 - (V_m \sin(\omega t))^2}{LV_{dc}\left(2I_o\right)}. \quad (6)$$

Note that for all three modulation methods, $T_1$ and $T_2$ are the required time for inductor current to traverse from the lower limit to the upper limit and from the upper limit to the lower

limit, respectively, and calculated as follows:

$$\begin{cases} T_1 = \dfrac{L\left(I_{\text{upper}} - I_{\text{lower}}\right)}{\left(V_{\text{dc}}/2\right) - V_{\text{grid}}} \\ T_1 = \dfrac{L\left(I_{\text{upper}} - I_{\text{lower}}\right)}{\left(V_{\text{dc}}/2\right) + V_{\text{grid}}} \end{cases}. \tag{7}$$

Switching frequency is derived from (7) as follows:

$$f_{\text{sw}} = \frac{\left(V_{\text{dc}}/2\right)^2 - \left(V_{\text{grid}}\right)^2}{LV_{\text{dc}}\left(I_{\text{upper}} - I_{\text{lower}}\right)}. \tag{8}$$

The switching frequency and inductor rms current are determined by the peak current boundaries. Figs. 3 and 4 depict the full load switching frequency and inductor rms current for each modulation method at different boundary values. An output inductor value of 270 $\mu$H was selected to ensure that the minimum switching frequency was above the maximum audible value of 20 kHz.

Referring to (2), (4), and (6), switching frequency for all three modulation methods is a function of the grid or output voltage and the peak current boundaries and is the highest at zero crossings. For example, BCM with fixed reverse current has the widest switching frequency range because both the instantaneous output voltage and the peak current boundaries decrease at zero crossings. BCM with fixed bandwidth has the narrowest switching frequency range since its peak current boundaries are constant over the entire output voltage range. Likewise, at full load, BCM with fixed reverse current has the lowest inductor rms current, while BCM with fixed bandwidth has the highest inductor rms current.

The minimum reverse current for achieving ZVS depends on the MOSFET's specification (parasitic capacitance, $C_{\text{OSS}}$), the voltage across the MOSFET $(V_{\text{dc}})$ and dead time $(t_d)$, and for this topology is approximately calculated as follows [14] and [15]:

$$I_{\text{min\_ZVS\_reverse\_current}} \approx \frac{2C_{\text{OSS}}V_{\text{dc}}}{t_d}. \tag{9}$$

An optimum combination of dead time (800 ns) and reverse current (0.8 A) was selected experimentally for this work. Therefore, in order to ensure ZVS operation for each modulation method, a minimum reverse current of 0.8 A is required to discharge the MOSFET parasitic capacitance. With this in mind, the minimum $I_o$ required to maintain the 0.8-A reverse current for each modulation method at full load is shown in Fig. 4. In all three modulation methods, ZVS is achieved during the entire grid cycle. Therefore, for each modulation $I_o$ is determined in such a way that ZVS can even be achieved for the lowest reverse current.

Since only turn-on ZVS can be achieved with these modulation methods, higher switching frequency generally results in proportionally higher switching losses. Larger boundary values reduce switching frequency but also increase inductor rms current and conduction losses.

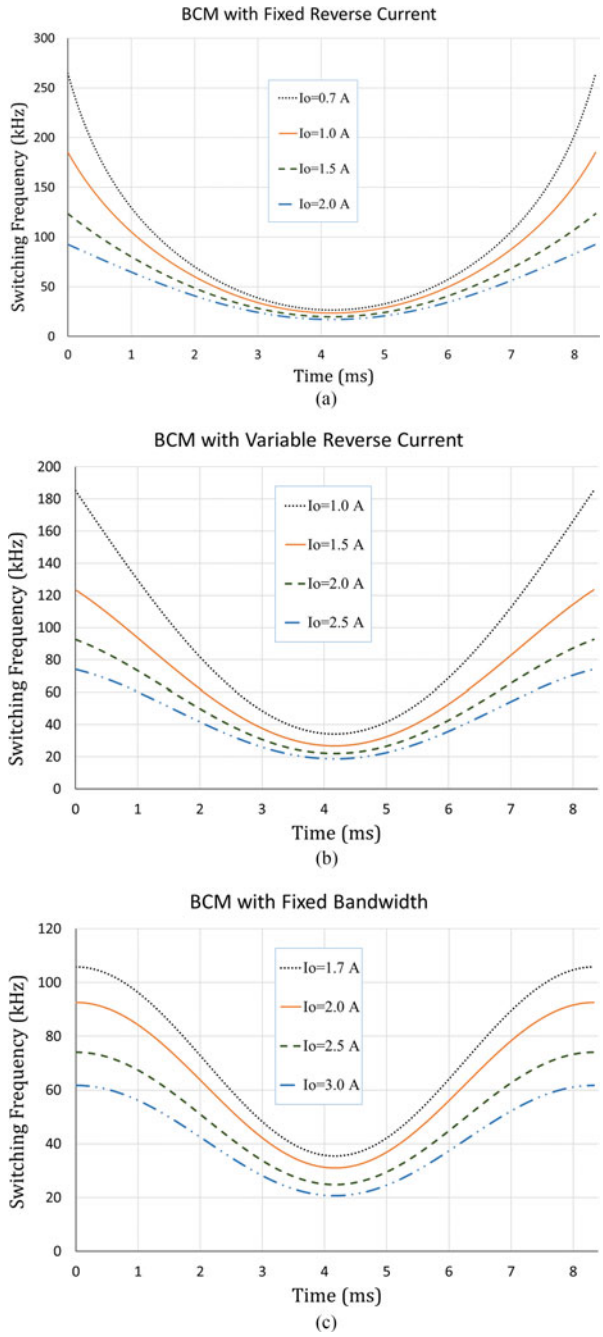


Fig. 3. Switching frequency over a half 60-Hz line cycle with varying $I_o$ for: (a) fixed reverse current, (b) variable reverse current, and (c) fixed band width.

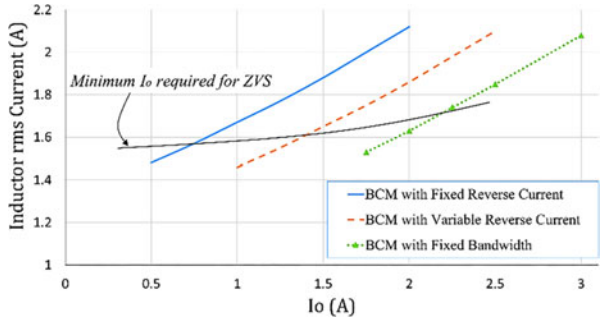


Fig. 4. Inductor rms current versus $I_o$ for each modulation method at full load.

TABLE I
INVERTER PROTOTYPE OPERATING PARAMETERS

| | |
|---|---|
| Grid parameters | $V_{\rm grid}$ (nominal) = 120 $V_{\rm rms}$ (Line-Neutral)<br>208 $V_{\rm rms}$ (Line-Line)<br>$f_{\rm grid}$ (nominal) = 60 Hz |
| Output power | $P_o$ = 130 W (each phase) |
| Input Voltage | $V_{\rm dc}$ = 400 V (+200 V, −200 V) |
| Switching devices | Fairchild FCB20N60F MOSFET |
| Output capacitor | $C_o$ = 1 $\mu$F polypropylene film (each phase) |
| Main inductor | $L$ = 270 $\mu$H (each phase), peak current = 4.5 A<br>$R_{\rm dc}$ = 85 m$\Omega$, magnetic core RM12/N95 ferrite, wire: Litz, 60 strands #38, 36.5 turns, air gap = 0.86 mm |

A detailed power loss analysis will be presented in the next section which determines the optimum boundary values for each modulation method in order to maximize efficiency.

## III. POWER LOSS ANALYSIS

A loss model was designed in order to predict the power loss in the three-phase half-bridge microinverter prototype. Table I shows the prototype operating parameters. This model can be used to calculate the most efficient peak current boundary for each of the three modulation methods. Four sources of loss have been taken into consideration in this model: switching loss (including MOSFET body diode conduction loss), MOSFET conduction loss, inductor core loss, and inductor winding loss.

Since all three modulation methods can achieve turn-on ZVS, only turn-off switching loss is calculated in the loss model using the following equation:

$$P_{\rm sw(OFF)}(t) = \frac{1}{2} \times I_i(t) \times V_{\rm DS} \times f_{\rm sw}(t) \times t_{s(H-L)} \quad (10)$$

where, $I_i$ $(i = 1, 2)$ is the peak boundary current for the upper and lower MOSFETs, respectively, $V_{\rm DS}$ is the MOSFET drain-source voltage, $f_{\rm SW}(t)$ is the instantaneous switching frequency and $t_{S(H-L)}$ is the MOSFET turn-off time.

To avoid shoot through current between the MOSFETs, dead time is included in the complementary gate drives. During the dead time, the MOSFETs body diode conducts which results in power loss and is calculated as follows:

$$P_{\rm BD}(t) = I_i(t) \times V_{\rm SD} \times f_{\rm sw}(t) \times (t_{d1} + t_{d2}) \quad (11)$$

where, $V_{\rm SD}$ is the diode forward voltage drop, $t_{d1}$ and $t_{d2}$ are the upper and lower MOSFET body diode conduction times, respectively.

MOSFET conduction loss is a function of the MOSFETs' on resistance and inductor rms current as follows:

$$P_{\rm conduction} = \frac{R_{\rm DS(ON)}}{T_S} \int_0^{T_s} {i_L}^2(t)\, dt \quad (12)$$

where, $R_{\rm DS(ON)}$ is the on-resistance of the MOSFET, $T_S$ is the switching period, and $i_{L(t)}$ is the instantaneous inductor current.

Since $I_i$ and $f_{\rm sw}$ change at each switching cycle, referring to (1)–(6), instantaneous values have been considered in the loss calculation. The losses are computed for each switching cycle and then averaged over the entire 60-Hz line cycle. For example, the upper MOSFET turn-off switching loss in BCM with fixed reverse current for a positive half cycle is calculated as follows:

$$P_{\rm upper\_sw(OFF)} = \frac{V_{\rm DS} \times t_{s(H-L)}}{T} \int_0^{\frac{T}{2}} (2I_{\rm REF}\sin(\omega t) + I_o) \times \frac{\left(V_{\rm dc}/2\right)^2 - (V_m \sin(\omega t))^2}{LV_{\rm dc}(2I_{\rm REF}\sin(\omega t) + 2I_o)} dt \quad (13)$$

where, $T$ is the 60-Hz line cycle period. Results were obtained using trapezoidal numerical integration in MATLAB.

The core geometry and winding parameters for the 270-$\mu$H inductor were input into the inductor core loss model in the MATLAB program [16]. The results were then incorporated into the power loss model presented in this paper. The loss model takes into account the varying switching frequency and core flux density to produce a more accurate core loss value. Winding losses consist of ac and dc losses. DC losses are simple function of inductor rms current and inductor dc resistance. AC losses are more complex and consist of skin effect and proximity effect, which are a function of switching frequency and ac inductor current and tend to greatly increase the ac resistance of the inductor winding. The ac resistance value is often many times that of the dc resistance. Note that since inductor current is bidirectional in all three modulation methods, there is no diode reverse recovery loss. Therefore, this loss is not included in the loss model.

Fig. 5 shows plots of efficiency as a function of peak current boundary at different output power levels for each of the three modulation methods. Efficiency is calculated using the loss model and plotted for various percentages of full load power for each modulation method. In BCM, with fixed reverse current, maximum efficiency is obtained when the peak boundary current is 0.8 A, as shown in Fig. 5(a). Peak current boundaries greater than the optimum value reduce the switching frequency and switching losses but increase the inductor rms current, MOSFET conduction losses, and AC winding losses. However, peak current boundaries smaller than the optimum value increase the switching frequency significantly, which causes increased inductor core loss. Similarly, in BCM with variable reverse current, the optimum peak current boundary changes slightly as power level increases and efficiency may be improved by dynamic adjustment of $I_o$, as depicted in Fig. 5(b).

In BCM with fixed bandwidth, the plot of efficiency as a function of peak current boundaries at different output power levels shows that maximum efficiency is achieved when the peak current boundary is close to the minimum $I_o$ required for ZVS as shown in Fig. 4. Fixed bandwidth modulation lends itself to dynamic adjustment of the peak current boundary based on the value of load current in order to further improve efficiency.

Note that for all three modulation methods, reducing the peak current boundaries below the minimum $I_o$ required for ZVS results in hard switching and significantly increased switching losses. Plots based on the power loss model show that each of the three modulation methods has a unique range of

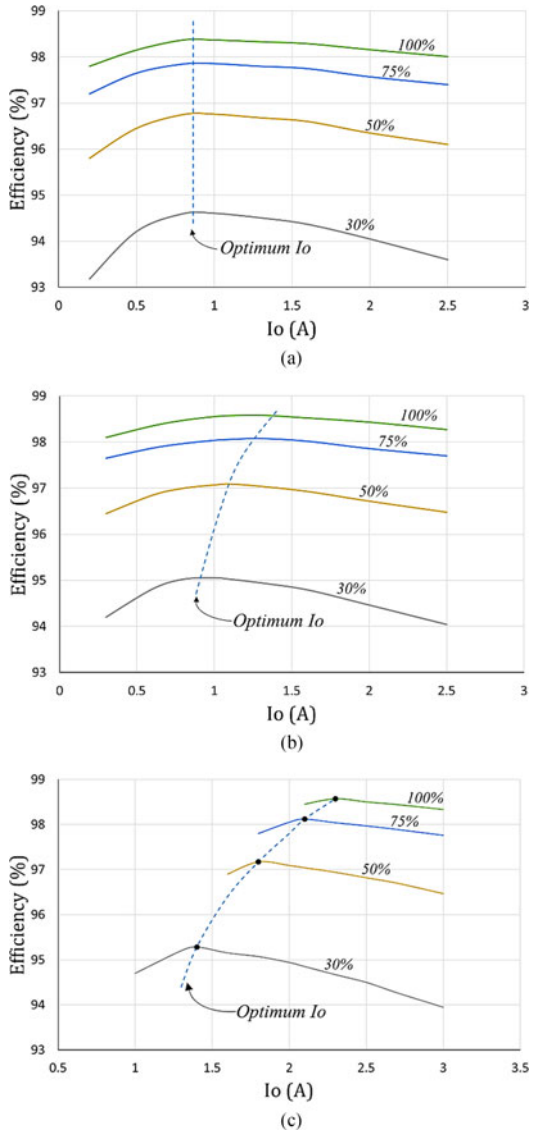


Fig. 5. Optimum peak current boundaries for three modulation methods at various power levels: (a) fixed reverse current, (b) variable reverse current, (c) fixed band width.

optimum $I_o$ value that will produce maximum efficiency for varying power levels. Notice that BCM with fixed reverse current and BCM with variable reverse current have a fairly narrow range of optimum $I_o$ values, while BCM with fixed bandwidth has a wide range of optimum $I_o$ values depending on the power level.

## IV. Proposed Dual-Zone Modulation

Based on the presented power loss model, a dual-zone modulation method is proposed to further improve efficiency [17]. This modulation method provides two main benefits: the addition of one more soft switching transition and low inductor peak current. The proposed dual-zone modulation method divides the 60-Hz waveform into two distinct zones each having its own peak current boundaries and switching frequency range. Fig. 6 shows the proposed dual-zone modulation method. Peak current boundaries and switching frequency for zone 1 can be

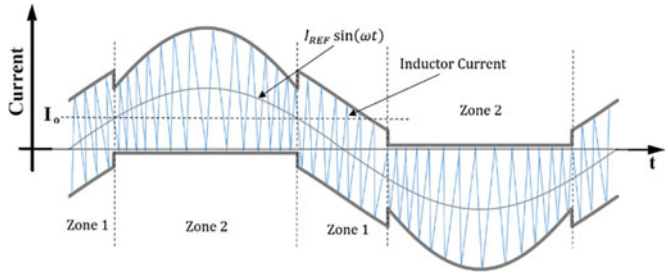


Fig. 6. Dual-zone modulation method.

determined as follows:

$$\begin{cases} I_{\text{upper}} = I_{\text{REF}} \sin(\omega t) + h \times I_o \\ I_{\text{lower}} = I_{\text{REF}} \sin(\omega t) - h \times I_o \end{cases}, \text{ if } |I_{\text{REF}} \sin(\omega t)| \le I_o \tag{14}$$

$$f_{\text{sw}}(t) = \frac{\left(V_{\text{dc}}/2\right)^2 - (V_m \sin\omega t)^2}{L V_{\text{dc}} (2h \times I_o)}. \tag{15}$$

Similarly, peak current boundaries and switching frequency for zone 2 are calculated as follows:

$$\begin{cases} I_{\text{upper}} = 2I_{\text{REF}} \sin(\omega t) \\ I_{\text{lower}} = 0 \end{cases}, \text{ if } I_{\text{REF}} \sin(\omega t) > I_o$$

$$\begin{cases} I_{\text{upper}} = 0 \\ I_{\text{lower}} = 2I_{\text{REF}} \sin(\omega t) \end{cases}, \text{ if } I_{\text{REF}} \sin(\omega t) < -I_o \tag{16}$$

$$f_{\text{sw}}(t) = \frac{\left(V_{\text{dc}}/2\right)^2 - (V_m \sin(\omega t))^2}{L V_{\text{dc}} (2I_{\text{REF}} \sin(\omega t))}. \tag{17}$$

Zone 1 is similar to fixed bandwidth modulation where turn-on ZVS can be achieved for both MOSFETs. The peak current boundaries are set by the value of $h$ as referenced in (14). Fig. 7(a) shows an expanded view of switching waveforms for zone 1. When the upper MOSFET (S1) is conducting, inductor current increases linearly until it crosses the upper boundary at that time it is turned OFF under hard switching. During the first dead time $(t_{d1})$, both MOSFETs are off and the inductor current completely discharges the lower MOSFET's parasitic capacitance, which provides turn-on ZVS for the lower MOSFET (S2). At the end of $t_{d1}$, the lower MOSFET is turned ON and the inductor current decreases linearly until it reaches the lower current boundary. The lower MOSFET is then turned OFF under hard switching and the second dead time $(t_{d2})$ begins. During $t_{d2}$, the inductor current completely discharges the upper MOSFET's parasitic capacitance that allows the upper MOSFET to be turned ON under ZVS. In zone 1, two of the four switching transitions are ZVS and the dead time intervals, $t_{d1}$ and $t_{d2}$, are almost equal.

Zone 2 resembles BCM with fixed reverse current modulation where both ZVS and zero current switching (ZCS) can be achieved. Fig. 7(b) illustrates an expanded view of switching waveforms for zone 2. When the inductor current crosses the upper boundary, the upper MOSFET (S1) is turned OFF under

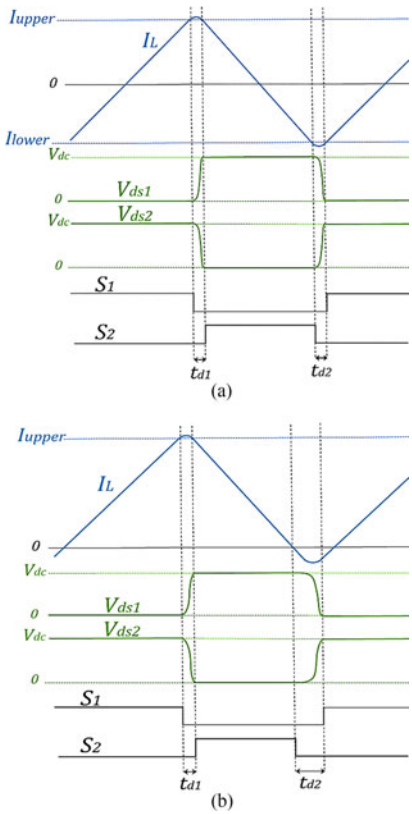


Fig. 7. Dual-zone modulation method switching waveforms: (a) Zone 1, (b) Zone 2.

hard switching. During the first dead time $(t_{d1})$, the inductor current completely discharges the lower MOSFET's parasitic capacitance that allows the lower MOSFET (S2) to be turned ON under ZVS. As the inductor current falls to zero, the lower MOSFET is turned OFF under ZCS. During the second dead time $(t_{d2})$, the inductor current becomes negative and completely discharges the upper MOSFET's parasitic capacitance. If $t_{d2}$ is sufficiently long so that the upper MOSFET's parasitic capacitance is completely discharged, the upper MOSFET can then be turned ON under ZVS. In zone 2, three of the four switching transitions are soft switched but unlike zone 1, the dead time intervals, $t_{d1}$ and $t_{d2}$, are quite different. Implementing dynamic dead time optimization (DDTO) [18] ensures that soft switching will be maintained in zone 2 over the entire operating range of the inverter.

The power loss model described in Section III has been used for the dual-zone modulation method to predict the optimum combination of $h$ and $I_o$ at various power levels. Fig. 8 shows plots of efficiency as a function of $h$ for different values of $I_o$ at 100% and 30% of rated power. At full load, maximum efficiency is achieved when $I_o$ and $h$ are 1.5 A and 1, respectively. At values of $h$ below 1, soft switching is not guaranteed over the entire 60-Hz line cycle and efficiency decreases significantly. However, at 30% of rated power, the power loss analysis shows that the total loss is lowest when the value of $h$ is greater than 1 for different values of $I_o$. Note that the values of $I_o$ and $h$ depend on the power level, with $h$ varying from 1.6 to 1 and $I_o$ varying from 0.7 to 1.5 A as shown in Fig. 8. In order to reduce

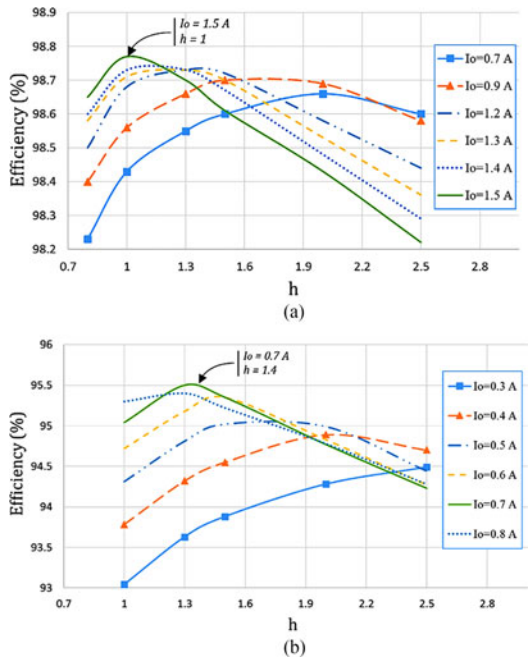


Fig. 8. Optimum peak current boundaries for dual-zone modulation method at (a) 100%, (b) 30% of rated power.

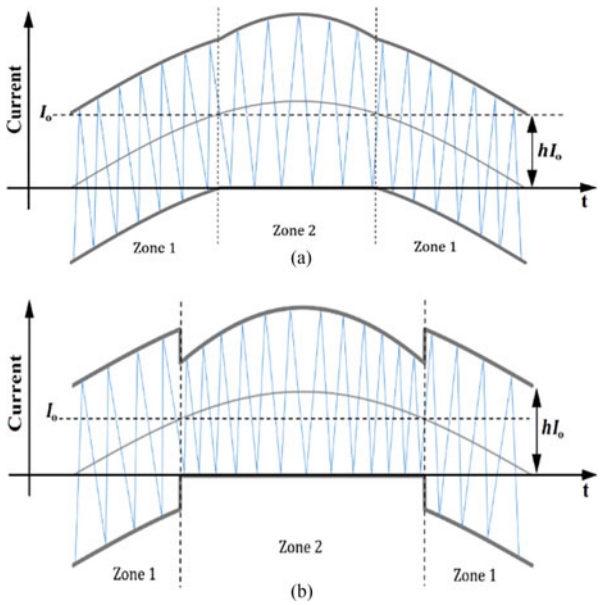


Fig. 9. Dual-zone peak current modulation at (a) high power, (b) low power.

computation time in the DSP, the optimum values of $I_o$ and $h$ were calculated using MATLAB for a range of power levels and placed in a lookup table in the DSP. The DSP then selects the values of $h$ and $I_o$ based on the inverter operating power.

Fig. 9 shows inductor peak current boundaries for high power and low power using dual-zone modulation. At high power, zone 1 is larger than zone 2 that reduces the overall switching frequency, while at low power, zone 2 is larger than zone 1, which reduces the inductor rms current. In the proposed control technique, inductor rms current and switching frequency are controlled according to the output power level. At high power

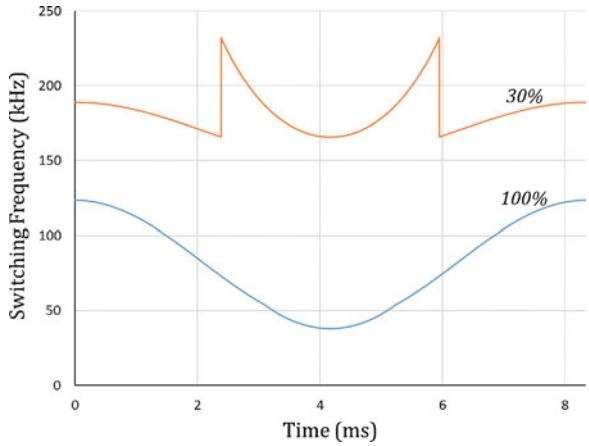


Fig. 10. Dual-zone modulation switching frequency range for 100% and 30% of rated power.

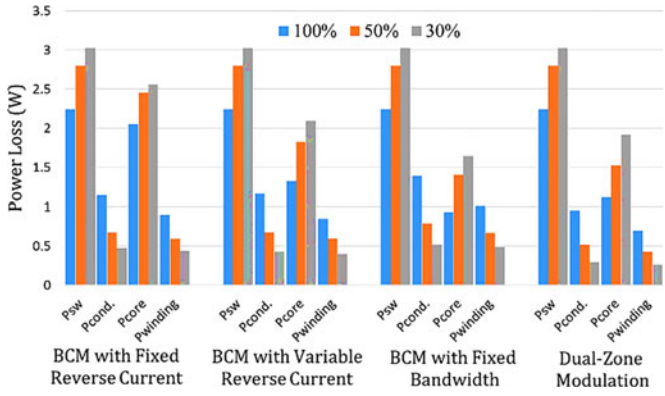


Fig. 11. Power loss distribution with different BCM modulation methods at 100%, 50%, and 30% of microinverter rated power.

levels, the switching frequency range is similar to the other three modulation methods. However, the inductor rms current is reduced resulting in lower conduction losses. At low power levels, the switching frequency range is higher than that of the other three modulation methods. However, the increased switching losses are offset by the addition of one more soft switching transition. Also, inductor rms current is lower than that of the other three modulation methods that results in lower conduction losses. The combination of the additional soft switching transition and reduced inductor rms current produces an overall improvement in efficiency. Dual-zone modulation switching frequency range for 100% and 30% of rated power for half a 60-Hz line cycle is shown in Fig. 10.

The power loss distribution for a 400-W three-phase half-bridge microinverter with four different BCM modulation methods is shown in Fig. 11. Since BCM with fixed bandwidth has the highest inductor rms current, MOSFET conduction losses and inductor winding losses are the highest with this modulation. However, MOSFET conduction losses and inductor winding losses are the lowest with dual-zone modulation because of its lower inductor rms current. Due to the fact that in BCM with fixed bandwidth, the peak current boundaries are constant over the entire 60-Hz line cycle, it has the narrowest switching frequency range and, therefore, the lowest inductor core loss.

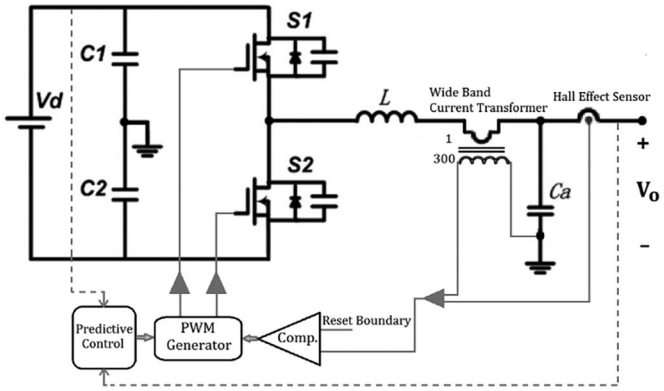


Fig. 12. DSP implementation of BCM peak current control.

Unlike BCM with fixed bandwidth, BCM with fixed reverse current modulation has the widest switching frequency range and, therefore, the highest inductor core loss due to the fact that switching frequency has a major impact on the inductor core loss calculation. As shown in Fig. 11, MOSFET switching losses are the largest portion of the total loss and increase as the output power level decreases. Although the peak current boundaries decrease at light loads in all of the modulation methods, the switching frequency increases significantly resulting in increased switching losses.

Although dual-zone modulation has a higher switching frequency in zone 2 compared with the other three modulation methods, the peak current boundaries are lower and it has one more soft switching transition. The lower peak current boundaries reduce MOSFET conduction losses and inductor winding losses thereby reducing overall power loss. Since the inductor peak current is low compared with the other three current modulation methods, the output filter inductor can be designed with fewer turns and a smaller gap that reduces inductor winding losses. Operating flux density can also be lower resulting in reduced core losses. The inductor could also be physically smaller, which improves power density and also has lower core loss due to the reduction in core volume.

## V. BCM Peak Current Control

Implementation of BCM peak current control for one phase in a DSP is shown in Fig. 12. In order to guarantee ZVS over the entire line cycle, the controller requires a precise measurement of the inductor current. Since the switching frequency varies over the 60-Hz line cycle and could go as high as 300 kHz depending on the modulation method used, inductor current cannot be accurately sampled using conventional A/D converters such as those found in digital signal controllers. To avoid this issue, the three-phase half-bridge microinverter prototype uses hybrid BCM current control [19], which is a combination of predictive control along with hardware reset. Predictive control calculates the duty cycle required for each operating point over the 60-Hz line cycle. Hardware reset is implemented by using the digital signal controller's internal high-speed comparators to terminate the on time once the peak current threshold has been crossed.

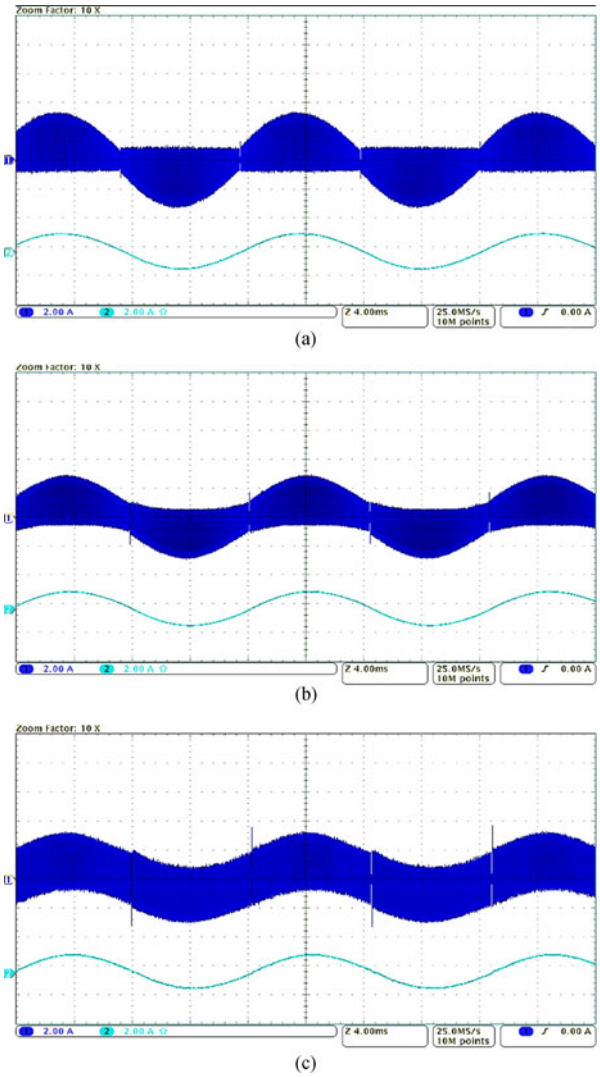


Fig. 13. Filter inductor current and output current for (a) BCM with fixed reverse current, (b) BCM with variable reverse current, (c) BCM with fixed bandwidth.

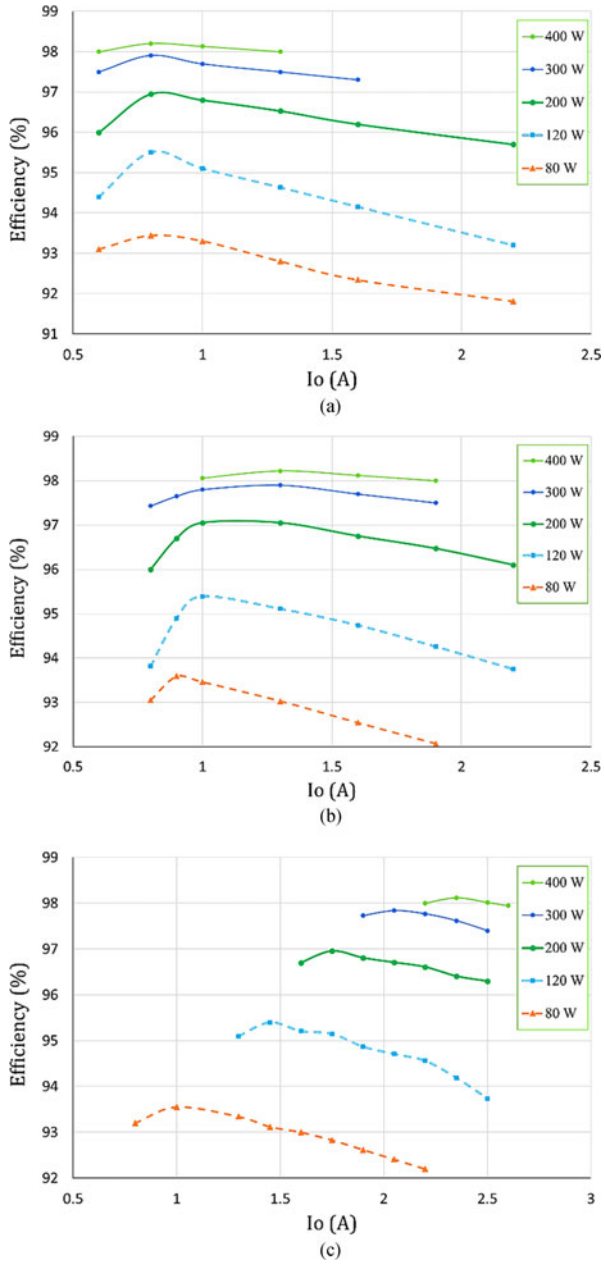


Fig. 14. Optimum peak current boundaries for three modulation methods at various power levels: (a) fixed reverse current, (b) variable reverse current, (c) fixed band width.

Hardware reset requires an accurate wide bandwidth current sensing circuit for measuring the inductor current. To accomplish this, a high-performance nanocrystalline core 300:1 current transformer was designed and included in the prototype. This current transformer exhibits zero-degree phase shift at 60 Hz while having an upper bandwidth limit of greater than 500 kHz and can easily reproduce the inductor current waveform with no distortion. The Hall effect sensor is only required to measure dc current to ensure that the output current has no dc component. The current transformer and Hall effect sensor outputs are combined to produce an accurate inductor current measurement, which is input to the high speed comparator inside the DSP.

## VI. Experimental Results

Experimental results were measured on a 400-W three-phase half-bridge microinverter prototype. The four previously discussed BCM modulation methods were implemented on a Microchip dsPIC33FJ16GS504. For the purpose of this experiment, the dc bus voltage was set to 400 V, the output inductor value was 270 $\mu$H for each phase, and the line frequency was 60 Hz. The microinverter was tested using BCM with fixed reverse current, BCM with variable reverse current and BCM with fixed bandwidth. The filter inductor high-frequency current and average current for each of the three modulation methods is shown in Fig. 13.

Fig. 14 shows the measured efficiency as a function of peak current boundary at different output power levels for each of the three modulation methods. Note that the empirical data closely resembles the efficiency calculated using the power loss model

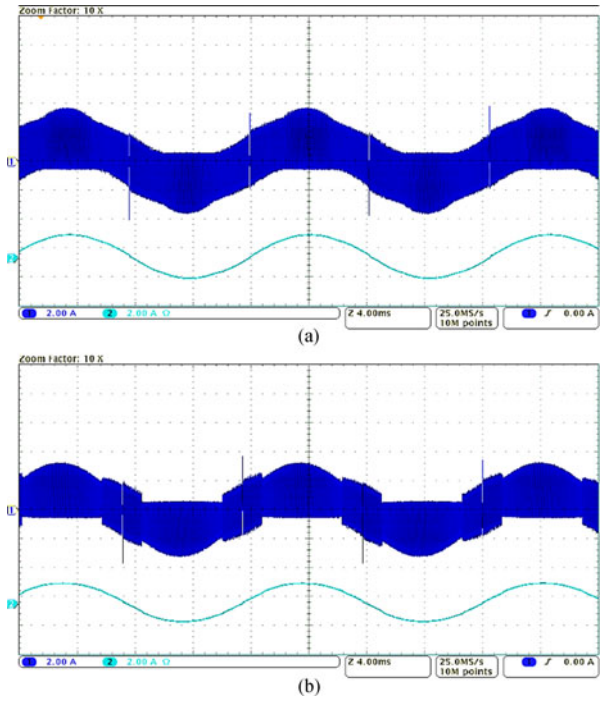


Fig. 15. Dual-zone peak current modulation at (a) high power, (b) low power.

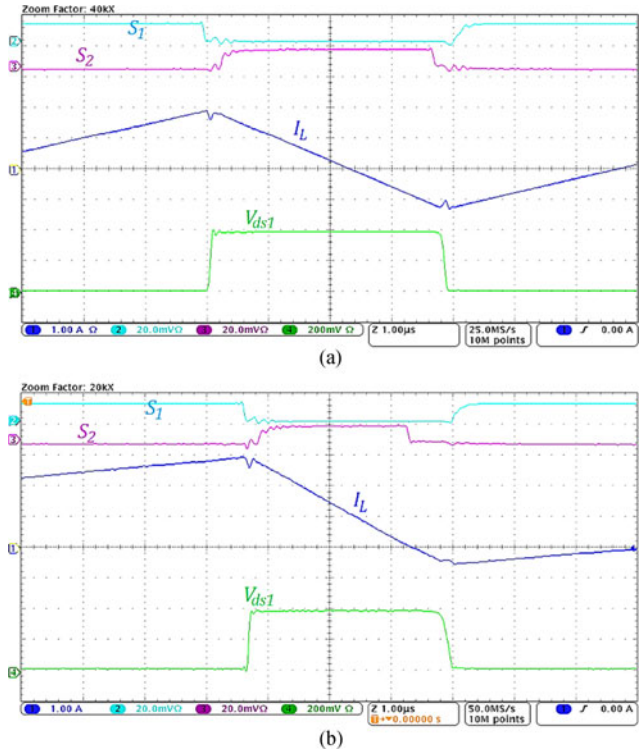


Fig. 16. Dual-zone modulation method switching waveforms: (a) Zone 1, (b) Zone 2.

shown in Fig. 5. The optimum $I_o$ measured on the prototype for each of the three modulation methods is almost identical to the calculated values. The experimental results at high power and high values of $I_o$ could not be obtained due to the saturation limit of the output filter inductor.

The filter inductor high-frequency current and average current in Fig. 15 were measured at high power and low power using the proposed dual-zone modulation technique. It can be seen that at high power, zone 1 is larger than zone 2, which reduces the overall switching frequency, while at low power, zone 2 is larger than zone 1, which reduces the inductor rms current. The switching waveforms for upper and lower MOSFETs in zone 1 and zone 2 were measured and are shown in Fig. 16. Referring to this figure in zone 1, the dead times are equal and turn-on ZVS is achieved for both MOSFETs. In zone 2, in addition to turn-on ZVS for both MOSFETs, turn-off ZCS is achieved for the lower MOSFET as shown in Fig. 16(b). The dead times are quite different due to the small amount of inductor current that is available to discharge the MOSFET's parasitic capacitance. The dead times in both zone 1 and zone 2 have been optimized over a 60-Hz line cycle using DDTO technique.

Fig. 17 shows the maximum efficiency for each of the modulation methods measured with a Yokogawa PZ4000 power analyzer. It can be seen that higher efficiency can be achieved using the proposed dual-zone modulation method without additional circuit components or cost. Total harmonic distortion (THD) is an important parameter to be considered when designing an inverter. Full power THD and inductor rms current for all four modulation methods are shown in Table II. Dual-zone modulation exhibits the lowest inductor rms current and its current THD is well within the limits specified by IEEE 1547.

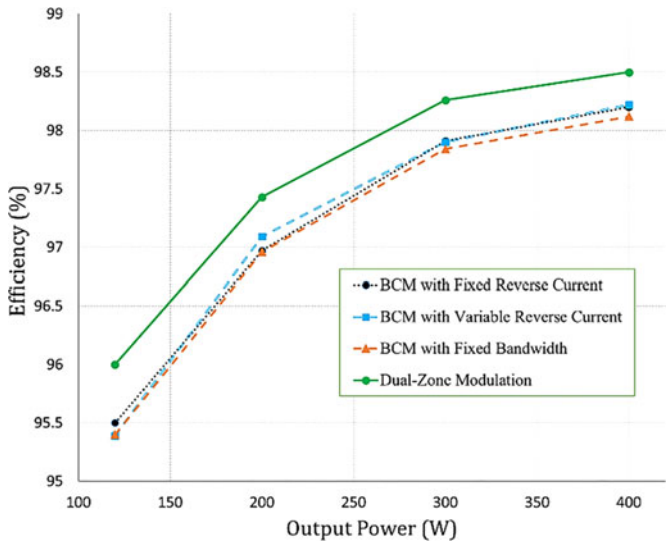


Fig. 17. Microinverter output stage efficiency with different modulation methods.

TABLE II
THD AND INDUCTOR RMS CURRENT FOR FOUR CURRENT MODULATION METHODS

| | THD | RMS |
|---|---|---|
| BCM with fixed reverse current | 2.5% | 1.59 |
| BCM with variable reverse current | 1.9% | 1.61 |
| BCM with fixed bandwidth | 1.4% | 1.76 |
| Dual-zone modulation | 2.4% | 1.45 |

## VII. Conclusion

In this paper, a precise power loss model has been presented to calculate the optimum peak current boundary for three different modulation methods: BCM with fixed reverse current, BCM with variable reverse current, and BCM with fixed bandwidth. The power loss analysis shows that the optimum peak current boundary is almost constant for BCM with fixed reverse current at different power levels, whereas it varies with load current for BCM with variable reverse current and BCM with fixed bandwidth. The experimental results on a 400-W three-phase half-bridge microinverter prototype verify the accuracy of the power loss model.

A dual-zone modulation method along with an improved control method have been proposed in this paper so as to further improve the efficiency of the microinverter prototype. Dual-zone modulation divides the 60-Hz waveform into two distinct zones. The power loss model was used to determine the size of each zone and calculate peak current boundaries. This modulation technique not only produces one more soft switching transition but also reduces inductor rms current, which results in an overall improvement in efficiency. In addition, dual-zone modulation produces the lowest inductor peak current compared with the other three modulation methods so that the output filter inductor can be a smaller and more efficient design with fewer turns and lower flux density. The improved peak current control method proposed in this paper consists of a wide-band current transformer that is accurate from 60 Hz to 500 kHz with zero-degree phase shift. The current transformer provides isolation and allows the entire inductor ac current waveform to be sensed.

## References


[1] C. Zheng *et al.*, "An optimization design for 5-kW centralized PV inverter to achieve 99% efficiency," in *Proc. IEEE Appl. Power Electron. Conf. Expo.*, 2013, pp. 2967–2970.

[2] S. Harb, M. Kedia, H. Zhang, and R. S. Balog, "Microinverter and string inverter grid-connected photovoltaic system—A comprehensive study," in *Proc. IEEE 39th Photovolt. Spec. Conf.*, 2013, pp. 2885–2890.

[3] X. Yaosuo, C. Liuchen, S. B. Kjaer, J. Bordonau, and T. Shimizu, "Topologies of single-phase inverters for small distributed power generators: An overview," *IEEE Trans. Power Electron.*, vol. 19, no. 5, pp. 1305–1314, Sep. 2004.

[4] J. M. A. Myrzik and M. Calais, "String and module integrated inverters for single-phase grid connected photovoltaic systems—A review," in *Proc. IEEE Power Tech Conf.*, Bologna, Italy, 2003, vol. 2, pp. 1–8.

[5] S. B. Kjaer, J. K. Pedersen, and F. Blaabjerg, "A review of single-phase grid-connected inverters for photovoltaic modules," *IEEE Trans. Ind. Appl.*, vol. 41, no. 5, pp. 1292–1306, Oct. 2005.

[6] W. Yu, J. Lai, H. Qian, and C. Hutchens, "High-efficiency MOSFET inverter with H6-type configuration for photovoltaic nonisolated AC-module application," *IEEE Trans. Power Electron.*, vol. 26, no. 4, pp. 1253–1260, Apr. 2011.

[7] B. Gu, J. Dominic, J. Lai, C. Chen, T. LaBella, and B. Chen, "High reliability and efficiency single-phase transformerless inverter for grid-connected photovoltaic systems," *IEEE Trans. Power Electron.*, vol. 28, no. 5, pp. 2235–2245, May 2013.

[8] M. R. Amini and H. Farzanehfard, "Three-phase soft-switching inverter with minimum components," *IEEE Trans. Ind. Electron.*, vol. 58, no. 6, pp. 2258–2264, Jun. 2011.

[9] M. Amirabadi, A. Balakrishnan, H. A. Toliyat, and W. Alexander, "Soft switched ac-link direct-connect photovoltaic inverter," in *Proc. IEEE Int. Conf. Sustain. Energy Technol.*, Nov. 2008, pp. 116–120.

[10] R. C. Beltrame, J. R. Zientarski, M. L. Martins, and J. R. Pinheiro, "Simplified zero-voltage-transition circuits applied to bidirectional poles: Concept and synthesis methodology," *IEEE Trans. Power Electron.*, vol. 26, no. 6, pp. 1765–1776, Jun. 2011.

[11] R. Li, Z. Ma, and D. Xu, "A ZVS grid-connected three-phase inverter," *IEEE Trans. Power Electron.*, vol. 27, no. 8, pp. 3595–3604, Aug. 2012.

[12] Y. Levron and R. W. Erickson, "High weighted efficiency in single-phase solar inverters by a variable-frequency peak current controller," *IEEE Trans. Power Electron.*, vol. 31, no. 1, pp. 248–257, Jan. 2016.

[13] Q. Zhang, H. Hu, D. Zhang, X. Fang, J. Shen, and I. Bartarseh, "A controlled-type ZVS technique without auxiliary components for the low power DC/AC inverter," *IEEE Trans. Power Electron.*, vol. 28, no. 7, pp. 3287–3296, Jul. 2013.

[14] S. M. Tayebi, X. Mu, and I. Batarseh, "Improved three-phase micro-inverter using dynamic dead time optimization and phase-skipping control techniques," in *Proc. IEEE Appl. Power Electron. Conf. Expo.*, Mar. 2016, pp. 1381–1386.

[15] S. M. Tayebi, N Kutkut, and I. Batarseh, "Effects of circuit nonlinearities on dynamic dead time optimization for a three-phase microinverter," in *Proc. IEEE Appl. Power Electron. Conf. Expo.*, Mar. 2017, pp. 1–5.

[16] Y. Levron, "Automatic design of inductors for power conversion," 2014. [Online]. Available at: http://www.mathworks.com

[17] S. M. Tayebi, N Kutkut, and I. Batarseh, "Analysis and optimization of BCM peak current mode control techniques for microinverters," in *Proc. IEEE Appl. Power Electron. Conf. Expo.*, Mar. 2017, pp. 1–8.

[18] S. M. Tayebi, C. Jourdan, and I. Batarseh, "Dynamic dead time optimization and phase-skipping control techniques for three-phase micro-inverter applications," *IEEE Trans. Ind. Electron.*, vol. 63, no. 12, pp. 7523–7532, Dec. 2016.

[19] D. Zhang, Q. Zhang, H. Hu, A. Crishina, J. Shen, and I. Batarseh, "High efficiency current mode control for three-phase micro-inverters," in *Proc. IEEE Energy Appl. Power Electron. Conf. Expo.*, Feb. 2012, pp. 892–897.



**S. Milad Tayebi** (S'09) received the B.S. degree in electrical engineering from Noshirvani University of Technology, Babol, Iran, and the M.S degree in electrical engineering, from Iran University of Science and Technology, Tehran, Iran in 2009 and 2012, respectively. He is currently working toward the Ph.D. degree in the Department of Electrical Engineering, University of Central Florida, Orlando, FL, USA.

He is currently at the Florida Power Electronic Center, University of Central Florida, Orlando, FL, USA. His current research interests include digital control in power electronics, efficiency optimization of dc/ac inverters, soft switching techniques, and multilevel inverters.



**Issa Batarseh** (F'06) received the B.S.E.E. degree in electrical and computer engineering, and the M.S. and Ph.D. degrees in electrical engineering from the University of Illinois, Chicago, IL, USA, in 1983, 1985, and 1990, respectively.

He is currently a Professor of electrical engineering in the School of Electrical Engineering and Computer Science, University of Central Florida (UCF), Orlando, FL, USA. From 1989 to 1990, he was a Visiting Assistant Professor with Purdue University, Calumet, IN, USA, before joining the Department of Electrical and Computer Engineering, UCF, in 1991. His research interests include power electronics, developing high-frequency energy conversion systems to improve power density, efficiency, and performance, the analysis and design of high-frequency solar and wind energy conversion topologies, and power factor correction techniques. He is the author or coauthor of more than 60 refereed journals and 300 conference papers in addition to 14 U.S. patents. He is also an author of a textbook entitled "*Power Electronic Circuits*" (New York: Wiley, 2003).

Dr. Batarseh is a Registered Professional Engineer in the State of Florida and a Fellow Member of the IEE. He has served as a Chairman for the IEEE Power Electronics Specialists Conference 07 and was the Chair of the IEEE Power Engineering Chapter, and the IEEE Orlando Section.